Cell Reports

Tumor-derived aminopeptidase N promotes early stages of brain metastatic colonization

Graphical abstract

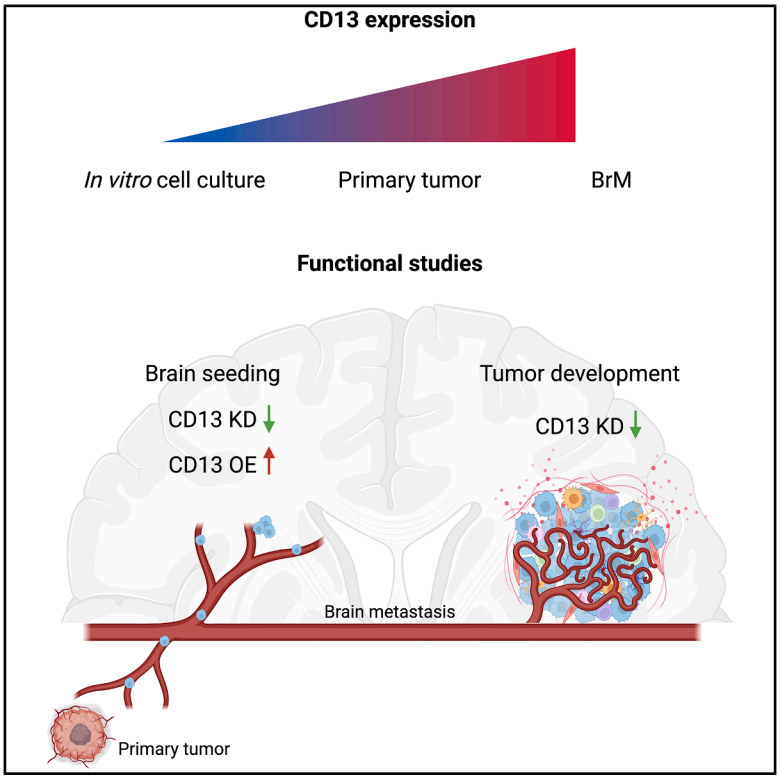

Highlights

- Cancer cells upregulate CD13 during brain metastasis
- Silencing CD13 delays metastatic progression and extends survival
- CD13 plays a role in cancer cell seeding in the brain
- Targeting CD13 offers a potential strategy against brain metastasis

Authors

Leire Bejarano, Alberto Hernández-Barranco, Vincent Roh, ..., Monika E. Hegi, Nadine Fournier, Johanna A. Joyce

Correspondence

leire.bejaranobosque@bio-gipuzkoa.eus (L.B.), johanna.joyce@unil.ch (J.A.J.)

In brief

In this study, Bejarano et al. show that the multifunctional enzyme CD13 is upregulated during brain metastasis and promotes cancer cell seeding across the blood-brain barrier. Loss of CD13 impairs brain colonization and prolongs survival in mice, highlighting CD13 as a potential therapeutic target in brain metastasis.

Bejarano et al., 2026, Cell Reports *45*, 116895
February 24, 2026
https://doi.org/10.1016/j.celrep.2025.116895

CellPress

Cell Reports

CellPress
OPEN ACCESS

Report

Tumor-derived aminopeptidase N promotes early stages of brain metastatic colonization

Leire Bejarano,[1,2,3,4,*] Alberto Hernández-Barranco,[1,2,3,4] Vincent Roh,[3,5] Rui Santalla Méndez,[1,2,3,4] Eleni Lamprou,[1,2,3,4] Catia F. Costa,[1,2,3,4] Michelle Ballabio,[1,2,3] Monika E. Hegi,[4,6,7] Nadine Fournier,[3,5] and Johanna A. Joyce[1,2,3,4,8,*]

[1]Department of Oncology, University of Lausanne, Lausanne, Switzerland
[2]Ludwig Institute for Cancer Research, University of Lausanne, Lausanne, Switzerland
[3]Agora Cancer Research Centre Lausanne, Lausanne, Switzerland
[4]Lundin Family Brain Tumor Research Center, Departments of Oncology and Clinical Neurosciences, Centre Hospitalier Universitaire Vaudois, Lausanne, Switzerland
[5]Translational Data Science Facility, Swiss Institute of Bioinformatics, Lausanne, Switzerland
[6]Department of Neurosurgery, Centre Hospitalier Universitaire Vaudois, Lausanne, Switzerland
[7]Neuroscience Research Center, Centre Hospitalier Universitaire Vaudois, Lausanne, Switzerland
[8]Lead contact
*Correspondence: leire.bejaranobosque@bio-gipuzkoa.eus (L.B.), johanna.joyce@unil.ch (J.A.J.)
https://doi.org/10.1016/j.celrep.2025.116895

SUMMARY

Metastasis is a highly inefficient process, with the vast majority of disseminated cancer cells failing to form secondary tumors. To establish brain metastases, cancer cells must traverse the blood-brain barrier and rapidly adapt to the specialized neural microenvironment. Here, we identify aminopeptidase N (CD13) as a pro-metastatic factor that supports the early stages of brain metastatic colonization. CD13 is upregulated in cancer cells during brain metastasis in both mouse models and human samples. CD13 knockdown significantly delayed metastatic growth and prolonged survival in mouse brain metastasis models while having no comparable effect on primary tumors. Loss- and gain-of-function experiments further revealed that CD13 enhances cancer cell seeding in the brain microenvironment. Together, these findings establish CD13 as an important mediator of brain metastatic colonization and a potential therapeutic target to prevent or delay disease progression.

INTRODUCTION

Brain metastasis (BrM) is the most common form of brain malignancy, arising primarily from lung cancer (40%–50%), breast cancer (BC) (15%–25%), and melanoma (5%–20%).[1–4] The metastatic cascade is a highly complex and inefficient process that involves cancer cell migration and invasion at the primary site, intravasation into the circulation, dissemination through the vascular system, and ultimately colonization of a distant organ.[5,6] For BrMs, one of the major bottlenecks in this cascade is the ability of cancer cells to adapt to the unique brain microenvironment.[6,7] This adaptation requires dynamic interactions with specialized tissue-resident cell types, including microglia, astrocytes, and neurons, as well as navigation through a distinct extracellular matrix (ECM) composition and, critically, the considerable challenge of traversing and co-opting the highly selective blood-brain barrier (BBB).[7]

The BBB is composed of four principal cellular elements: endothelial cells (ECs), pericytes, astrocytic endfeet, and associated microglial cells.[8,9] Cancer cells exploit diverse strategies to penetrate this barrier, including proteolytic processing of junctional adhesion molecules[10] and expression of factors that promote BBB transmigration, such as CTSS,[10] PLEKHA5,[11] PTSG2, HB-EGF, ST6GALNAC5,[12] and PLGF.[13] Once within the brain, metastatic cells often grow and survive through attachment along existing blood vessels—a process termed vascular co-option—which is supported by cell adhesion molecules such as L1CAM.[14] Notably, different BC subtypes, including triple-negative BC (TNBC) and HER2-positive tumors, display distinct patterns of vascular interaction during early brain colonization, resulting in varied tumor architectures.[15] Moreover, metastatic cancer cells can evade BrM-suppressive mechanisms, such as plasmin-mediated degradation, through the expression of serpin proteins.[14] Despite these insights, BrM remains incurable, underscoring the critical need to identify additional mechanisms that enable metastatic cancer cells to adapt, survive, and expand within the brain parenchyma.

One such candidate is aminopeptidase N, also known as CD13, which is a membrane-bound metalloprotease expressed by various cell types, including cancer cells, immune cells, and cells within the angiogenic vasculature.[16,17] High CD13 expression correlates with poor prognosis in several cancers, including colon[18] and non-small cell lung cancer,[19] among others.[16] Through its enzymatic activity, CD13 modulates the function of various bioactive peptides, including endorphins, enkephalins, and angiotensin III.[16,17] Beyond its peptidase function, CD13 acts as a "moonlighting" enzyme,[16,17] with roles in cell adhesion, migration, invasion, angiogenesis,[20] and integrin recycling.[21]

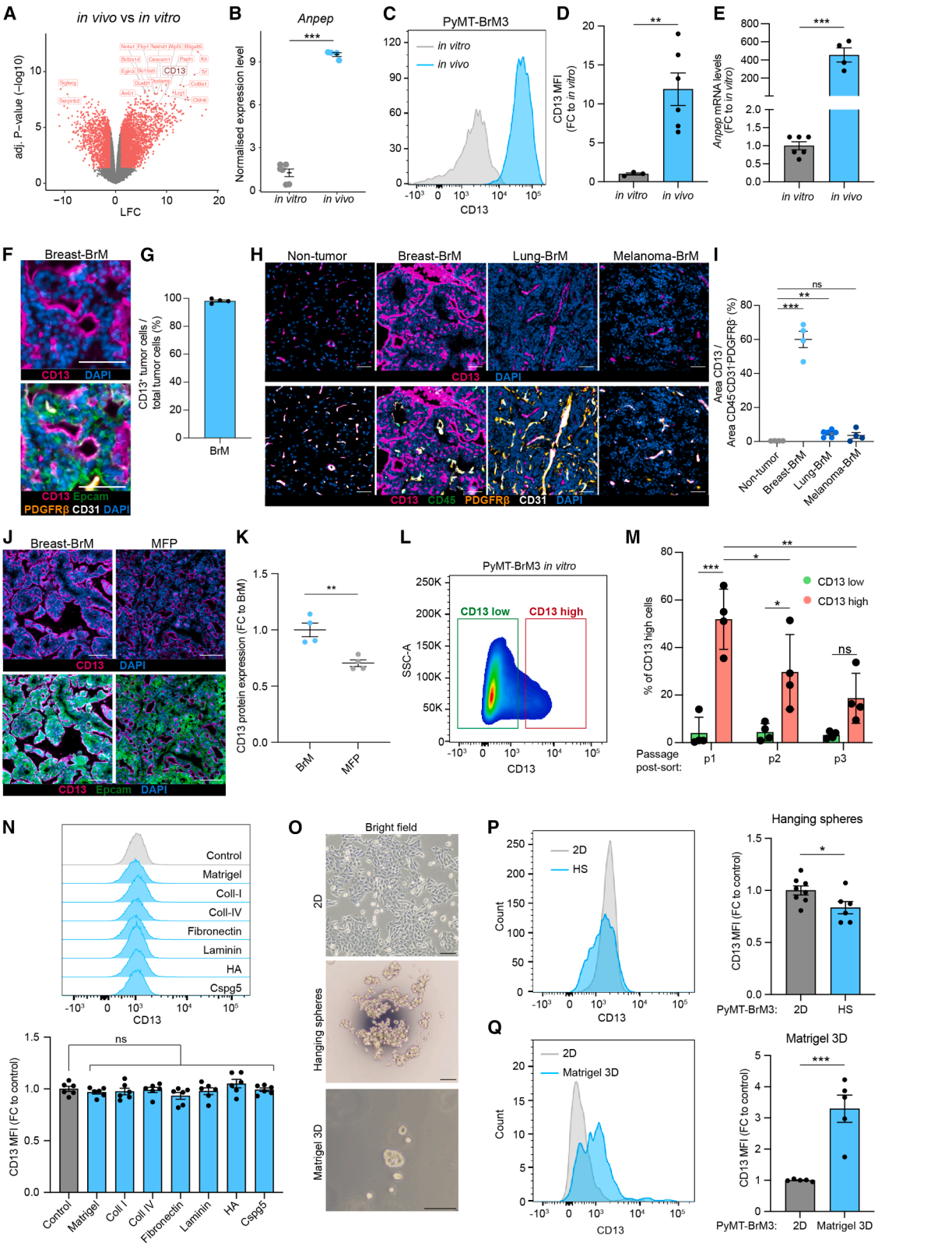

(legend on next page)

These diverse functions make CD13 a compelling candidate mediator of brain metastatic colonization and a potential therapeutic target. However, its role in BrM has not been previously explored. In this study, we investigate CD13 in clinical samples and preclinical models to investigate its contribution to metastatic seeding and growth in the brain.

RESULTS

CD13 overexpression is induced *in vivo* in mouse breast-BrM

To investigate the changes that occur in cancer cells during the process of metastatic colonization, we performed RNA sequencing (RNA-seq) analysis comparing the brain-homing PyMT-BrM3 cell line cultured *in vitro* with PyMT-BrM3 cells freshly isolated from established metastases in syngeneic mice (C57BL/6J background). PyMT-BrM3 cells originate from the transgenic MMTV-PyMT breast primary tumor model and were enriched for brain tropism through three rounds of *in vivo* passaging.[22] BrMs were induced by intracardiac injection of the brain-homing cells, and this model faithfully recapitulates multiple stages of the metastatic cascade.[22]

Differential expression analysis (*in vivo* vs. *in vitro*) was performed, and we queried the top differentially expressed genes (DEGs) for targetable candidates that could drive metastatic colonization (Table S1). We found that *Anpep* (encoding the CD13 protein) was significantly upregulated in the *in vivo* BrM condition (Figures 1A and 1B). This finding was validated by flow cytometry, which showed significantly higher CD13 levels in PyMT-BrM3 cells harvested directly from intracardially generated *in vivo* BrMs compared with *in vitro* cultures (Figures 1C and 1D), and was further confirmed by quantitative reverse-transcription PCR (RT-qPCR) (Figure 1E). Additional immunofluorescence (IF) analysis of tissue sections using antibodies recognizing EpCAM (tumor cells), CD31 and PDGFRβ (endothelial and mural cells, respectively), and CD13 revealed that ∼98% of tumor cells expressed CD13 in the breast-BrM model (Figures 1F and 1G). We also found that CD13 protein levels were lower in perivascular regions compared with non-perivascular tumor areas (Figure S1A).

We next examined whether CD13 is also upregulated in BrM models of lung (Sv2T3-BrM1) and melanoma (Yumm1.1-BrM4) primary origin,[23,24] using the breast-BrM model as a positive control. IF analysis distinguished CD13 expression across different cell types by using CD31 and PDGFRβ as above, CD45 as a pan-immune cell marker, and defining $CD31^{-}PDGFR\beta^{-}CD45^{-}$ cells as cancer cells (Figure 1H). CD13 was highly expressed in cancer cells from the breast-BrM model *in vivo*, but not in lung- or melanoma-derived BrMs (Figure 1I). We also evaluated CD13 in primary breast tumors generated by injecting tumor cells into the mammary fat pad (MFP). While MFP tumors expressed CD13 (Figure 1J), the levels were significantly higher in breast-BrMs (Figure 1K), as validated by RT-qPCR (Figure S1B).

PyMT-BrM3 cells grown *in vitro* contained a $CD13^{high}$ subpopulation (Figure 1L). We sorted both $CD13^{high}$ and $CD13^{low}$ PyMT-BrM3 populations from the parental cell line and cultured them separately for several passages. In the first passage post-sort, $CD13^{high}$ cells retained elevated CD13 expression, but this difference progressively diminished over successive passages (Figures 1M and S1C), indicating that standard *in vitro* conditions are insufficient to sustain high CD13 expression. Based on these findings, we next investigated whether CD13 expression could be modulated by extrinsic environmental cues. Focusing on breast-BrM cells, we compared CD13 levels under different *in vitro* conditions, including plating cells on diverse ECM substrates, culturing as hanging spheres, or embedding in

Figure 1. Aminopeptidase N/CD13 expression in mouse BrM

(A) Volcano plot of DEGs in PyMT-BrM3 tumors *in vivo* ($n = 6$ independent samples) vs. *in vitro* PyMT-BrM3 cell cultures ($n = 4$ samples). CD13 is highlighted in the plot.
(B) Normalized counts of *Anpep* (encoding CD13) in PyMT-BrM3 tumors *in vivo* ($n = 6$) vs. PyMT-BrM3 cells *in vitro* ($n = 4$).
(C) Representative histogram of CD13 protein expression analyzed by flow cytometry in PyMT-BrM3 cells *in vitro* vs. *in vivo*.
(D) Flow cytometry quantification of CD13 mean fluorescence intensity (MFI) in PyMT-BrM3 cells *in vitro* ($n = 3$) vs. *in vivo* ($n = 6$); FC = fold change.
(E) *Anpep* mRNA levels measured by RT-qPCR in PyMT-BrM3 cells *in vitro* ($n = 6$) vs. *in vivo* ($n = 4$).
(F) Representative IF images of CD13, Epcam (cancer cells), CD31 (ECs), and PDGFRβ (mural cells), and 4′,6-diamidino-2-phenylindole, dihydrochloride (DAPI) (cell nuclei) in murine breast-BrM tissue. Scale bars, 50 μm.
(G) Quantification of $CD13^{+}$ cancer cells as a percentage of total cancer cells (defined as $Epcam^{+}$; $CD31^{-}$; $PDGFR\beta^{-}$ cells) in breast BrM ($n = 4$).
(H) Representative IF images of CD13, CD31, PDGFRβ, CD45, and DAPI in mouse non-tumor brain samples and BrMs from breast, lung, or melanoma primary origin. Scale bars, 50 μm.
(I) Quantification of $CD13^{+}$ area in the $CD31^{-}PDGFR\beta^{-}CD45^{-}$ population (cancer cells) in mouse non-tumor brain tissue samples ($n = 4$) and BrMs from breast ($n = 4$), lung ($n = 6$), or melanoma ($n = 4$) primary origin.
(J) Representative IF images of CD13, EpCAM, and DAPI in murine breast-BrM and MFP tumors. Scale bars, 100 μm.
(K) Quantification of CD13 protein expression in breast-BrM ($n = 4$) and MFP tumors ($n = 4$). Data are represented as mean ± SEM.
(L) Representative flow cytometry plots of CD13 expression in sorted $CD13^{low}$ and $CD13^{high}$ PyMT-BrM3 cells across passages P1–P3 after sorting.
(M) Quantification of the percentage of $CD13^{high}$ cells in passages P1–P3 after sorting ($n = 4$).
(N) Representative histogram (upper panel) and quantification (lower panel) of CD13 MFI in PyMT-BrM3 cells cultured *in vitro* on different ECM substrates ($n = 6$).
(O) Representative bright-field images of PyMT-BrM3 cells cultured in 2D, as hanging spheres, or in 50% Matrigel 3D. Scale bars, 100 μm.
(P) Representative histogram (left) and quantification (right) of CD13 MFI in 2D cultures ($n = 8$) vs. hanging sphere cultures ($n = 6$).
(Q) Representative histogram (left) and quantification (right) of CD13 MFI in 2D cultures ($n = 5$) vs. 50% Matrigel 3D cultures ($n = 5$).
In (B), (D), (E), (G), (I), (K), (M), (N), (P), and (Q), data are represented as mean ± SEM. Each dot represents a biological replicate. *P.adj* values from differential expression analysis using limma were used in (B). Unpaired two-tailed *t* tests were used in (D), (E), (K), (P), and (Q). An ANOVA test ($p < 0.0001$), followed by an unpaired two-tailed *t* test with Bonferroni correction for multiple comparisons, was used in (I). A two-way ANOVA followed by Sidak's multiple comparison test was used in (M). An ANOVA/Kruskal-Wallis test ($p = 0.4569$), followed by a Mann-Whitney two-tailed test with Bonferroni correction for multiple comparisons, was used in (N).
P.adj values are reported in (B), (I), (M), and (N), and *p* values are reported in (D), (E), (K), (P), and (Q): $^{*}p < 0.05$, $^{**}p < 0.01$, $^{***}p < 0.001$, ns = non-significant.
See also Figure S1 and Table S1.

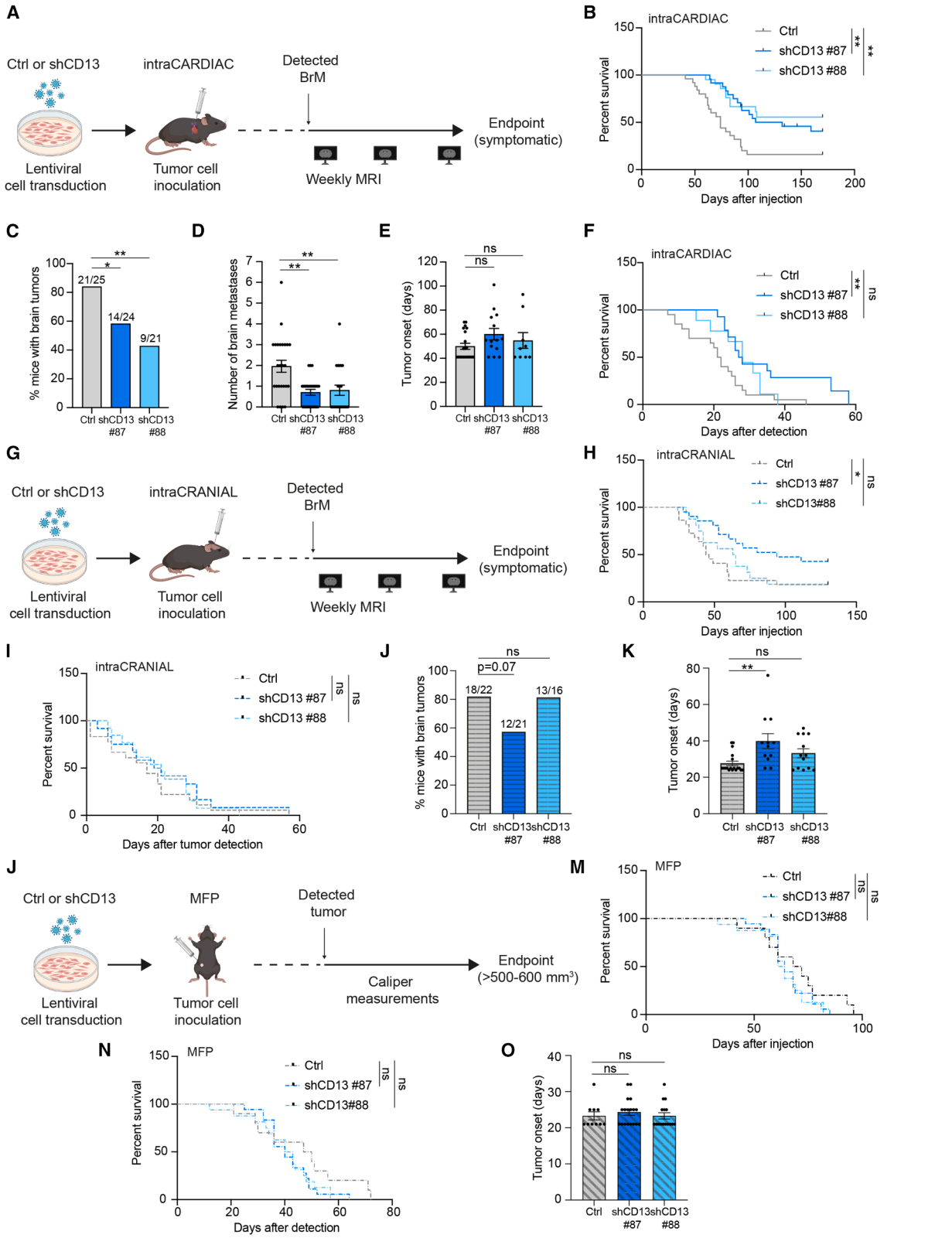

(legend on next page)

Matrigel. For ECM induction, PyMT-BrM3 cells were plated on various substrates, including Matrigel (1%), collagen-I (Coll-I, 100 μg/mL), collagen IV (Coll-IV, 100 μg/mL), fibronectin (40 μg/mL), laminin (40 μg/mL), hyaluronic acid (100 μg/mL), and CSPG5 (1 μg/mL). None of these coatings significantly upregulated CD13 under 2D culture conditions (Figure 1N). We then examined whether 3D culture might induce CD13 expression by growing PyMT-BrM3 cells either as hanging spheres for 12 h (30 μL drops in an inverted Petri dish) or embedded in 50% Matrigel for 1 week (Figure 1O). Notably, only Matrigel culture led to a significant CD13 increase (Figures 1P and 1Q), suggesting that matrix-derived mechanical forces or biochemical signals may contribute to CD13 induction *in vivo*.

CD13 knockdown delays BrM but not primary tumor growth

Given its elevated expression in human and mouse BrM, we next evaluated the functional role of CD13 in metastatic progression. PyMT-BrM3 cells were transduced with two independent short hairpin RNAs (shRNAs) targeting CD13 (shCD13 #87 and #88). or a non-targeting control. Knockdown efficiency was confirmed (Figure S2A), and cell proliferation *in vitro* was unaffected (Figure S2B). Because CD13 expression is low under standard culture conditions (Figures 1B–1E), we generated CD13-overexpressing (PyMT-BrM3-CD13-OE) cells and subsequently introduced either of the two independent shRNAs or the non-targeting control into this background. In this context, CD13 knockdown was similarly efficient (Figure S2C).

We then performed intracardiac injections of PyMT-BrM3 cells—transduced with shCD13 #87, shCD13 #88, or the non-targeting control—into C57BL/6J mice and monitored BrM progression by magnetic resonance imaging (MRI) until symptom onset (Figures 2A and S2D). CD13 knockdown significantly prolonged mouse survival (Figure 2B) and reduced both BrM incidence (Figure 2C) and the number of metastases per mouse (Figure 2D). Tumor onset, however, was not affected (Figure 2E). Analysis of mouse survival following the initial BrM detection also indicated a survival benefit with CD13 knockdown, which was significant for shCD13 #87 and showed a positive trend for shCD13 #88 (Figure 2F).

To determine whether CD13 knockdown also influences tumor outgrowth when the early stages of metastasis are bypassed, we directly injected shCD13 or control PyMT-BrM3 cells into the brain (intracranial injection) and monitored tumor volume by MRI over time (Figure 2G). In this setting, we observed prolonged overall survival with shCD13 #87 (Figures 2H and S2E), but no significant differences in survival after tumor detection (Figures 2I and S2E). We also observed a modest decrease in tumor incidence and delayed tumor onset with shCD13 #87 (Figures 2J and 2K).

Finally, to assess whether CD13 knockdown also impacts primary tumor growth, we injected control or shRNA-transduced PyMT-BrM3 cells into the MFP of C57BL/6J mice (Figure 2L). Tumor growth was assessed by caliper measurements until tumors reached >500–600 mm^3 (Figure S2F). In this setting, CD13 knockdown did not alter survival, tumor

Figure 2. CD13 knockdown in brain metastasis and primary tumors

(A) Experimental design for cell transduction, intracardiac BrM tumor induction, and MRI monitoring.

(B) Kaplan-Meier survival curves of mice intracardially injected with control (n = 25) or CD13 knockdown (shCD13 #87, n = 24; shCD13 #88, n = 21) PyMT-BrM3 cells. Curves represent animal survival after cancer cell injection. Statistical analysis was performed using the log-rank (Mantel-Cox) test.

(C) Percentage of mice with BrM tumors following injection with control or CD13 knockdown cells ($n_{Control}$ = 25, n_{sh87} = 24, n_{sh88} = 21). The chi-square test was used for statistical analysis.

(D) Number of brain metastases in mice injected with control or CD13 knockdown cells ($n_{Control}$ = 25, n_{sh87} = 24, n_{sh88} = 21). Data are represented as mean ± SEM. Each dot represents an individual mouse. An ANOVA/Kruskal-Wallis test (p = 0.0012) was performed, followed by a Mann-Whitney two-tailed test with the Bonferroni correction method.

(E) BrM tumor onset (days) in mice injected with control or CD13 knockdown cells ($n_{Control}$ = 21, n_{sh87} = 14, n_{sh88} = 9). Data are represented as mean ± SEM. Each dot represents an individual mouse. An ANOVA/Kruskal-Wallis test (p = 0.1374) was used, followed by the Mann-Whitney two-tailed test with Bonferroni correction for multiple comparisons.

(F) Kaplan-Meier survival curves of mice intracardially injected with control or CD13 knockdown cells ($n_{Control}$ = 20, n_{sh87} = 14, n_{sh88} = 9). Curves represent survival after BrM tumor detection. Statistical analysis was performed using the log-rank (Mantel-Cox) test.

(G) Experimental design for cell transduction, intracranial BrM tumor induction, and MRI monitoring.

(H and I) Kaplan-Meier survival curves of mice intracranially injected with control or CD13 knockdown PyMT-BrM3 cells. (H) Curves represent survival after cancer cell injection ($n_{Control}$ = 22, n_{sh87} = 21, n_{sh88} = 16), and (I) survival after BrM tumor detection ($n_{Control}$ = 18, n_{sh87} = 12, n_{sh88} = 13). The log-rank (Mantel-Cox) test was used for statistical analysis.

(J) Percentage of mice with BrM tumors in mice injected with control or CD13 knockdown cells ($n_{Control}$ = 22, n_{sh87} = 21, n_{sh88} = 16). The chi-square test was used for statistical analysis.

(K) BrM tumor onset (days) in mice injected with control or CD13 knockdown cells ($n_{Control}$ = 18, n_{sh87} = 12, n_{sh88} = 13). Data are represented as mean ± SEM. Each dot represents an individual mouse. The ANOVA/Kruskal-Wallis test p = 0.0076 was used, followed by a Mann-Whitney two-tailed test with the Bonferroni correction method.

(L) Experimental design for cell transduction, mammary fat pad (MFP) tumor induction, and MRI monitoring.

(M and N) Kaplan-Meier survival curves of mice injected in the MFP with control or CD13 knockdown PyMT-BrM3 cells ($n_{Control}$ = 10, n_{sh87} = 18, n_{sh88} = 16). Curves represent survival after cancer cell injection in (M) and survival after detection in (N). The log-rank (Mantel-Cox) test was used for statistical analysis.

(O) Primary MFP tumor onset (days) in mice injected with control or CD13 knockdown cells in the MFP ($n_{Control}$ = 10, n_{sh87} = 18, n_{sh88} = 16). Data are represented as mean ± SEM. Each dot represents an individual mouse. The ANOVA/Kruskal-Wallis test p = 0.5720 was used, followed by a Mann-Whitney two-tailed test with the Bonferroni correction method.

The subscript in the n value indicates the experimental condition. *P.adj* values in (D), (E), (K), and (O) and p values in (B), (C), (F), (H), (I), (J), (M), and (N): $^*p < 0.05$, $^{**}p < 0.01$, ns = non-significant.

See also Figures S2 and S3.

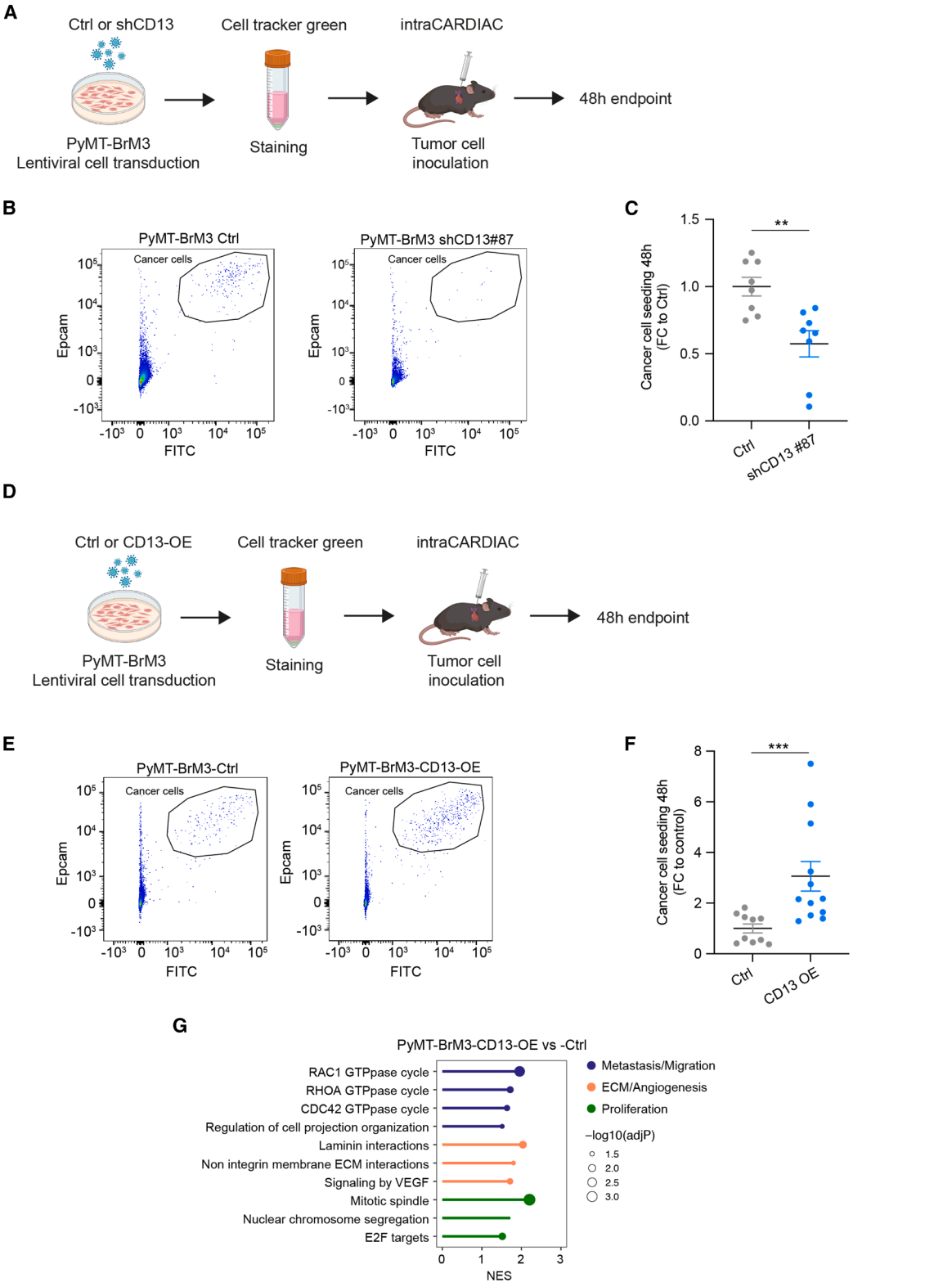

Figure 3. Cancer cell seeding upon CD13 knockdown and CD13 overexpression

(A) Experimental design for cell transduction, cell labeling, and intracardiac cell injection in loss-of-function cell seeding assays.

(B) Representative flow cytometry plots of control and CD13 knockdown cancer cells in the brain (total cell suspension) 48 h after intracardiac injection, defined by Epcam+FITC+ staining.

(legend continued on next page)

onset, or growth kinetics (Figures 2M–2O). Collectively, these results indicate that the functional role of CD13 is specific to breast-BrM and does not extend to primary tumor development.

CD13 knockdown does not affect the tumor microenvironment

Given that CD13 knockdown markedly affected BrM progression following intracardiac injection, we next evaluated its impact on the tumor microenvironment (TME) in this setting. IF staining confirmed efficient CD13 suppression in the tumors at endpoint for both shCD13 constructs (Figures S2G and S2H). To assess potential alterations in the immune cell compartment, we performed IF for CD45 (total immune cells), Iba1 (macrophages), CD3 (total T cells), and CD8 (cytotoxic T cells) (Figure S3A). Quantification of these immune populations revealed no significant differences between control and CD13-knockdown tumors (Figures S3B–S3E).

Because CD13 has recognized roles in angiogenesis in other contexts,[16–18,20] we also analyzed vascular features by staining for CD31 and extravascular fibrinogen as a readout of vessel leakiness[25] (Figure S3A). Similar to the immune cell analysis, we observed no significant differences in vessel size (Figure S3F), vessel area (Figure S3G), or extravascular fibrinogen levels (Figure S3H) between groups. Finally, we assessed tumor proliferation by Ki67 staining (Figure S3A), which revealed no difference in the percentage of proliferating cells upon CD13 knockdown (Figure S3I). Collectively, these results indicate that the anti-metastatic effects of CD13 depletion are independent of alterations to the TME or proliferative capacity and suggest that CD13's predominant role occurs during the metastatic seeding phase.

CD13 plays a role in early cancer cell seeding

Considering the BrM-specific effects of CD13 knockdown (Figure 2) and the absence of detectable changes in the TME of tumors at endpoint (Figure S3), we hypothesized that CD13 might act during the early stages of brain metastatic seeding. To test this, control and CD13-knockdown PyMT-BrM3 cells were labeled with a fluorescent cell tracker dye and injected intracardially into C57BL/6J mice. Mice were sacrificed 48 h post-injection, brains were digested, and cancer cells were quantified by flow cytometry (Figure 3A). Immune cells were excluded using CD45 and CD11b markers (gating on the $CD45^-$ $CD11b^-$ population), and the brain-seeded cancer cells were identified by cell tracker fluorescence (fluorescein isothiocyanate [FITC]) and the epithelial cell marker EpCAM. Notably, CD13 knockdown significantly reduced the percentage of cancer cells detected in the brain (Figures 3B and 3C).

To further validate the role of CD13 in early seeding, we used the CD13-overexpressing PyMT-BrM3-CD13-OE cells. CD13 expression was confirmed by flow cytometry (Figure S4A), and overexpression did not alter *in vitro* growth (Figure S4B). We applied the same experimental strategy as above—cell labeling, intracardiac injection, and analysis 48 h later (Figure 3D). Consistent with the knockdown results, CD13 overexpression significantly increased the proportion of brain-seeded cells (Figures 3E and 3F). To gain insight into the mechanisms underlying this enhanced brain seeding, we performed RNA-seq comparing CD13-OE cells and control cells. Gene set enrichment analysis (GSEA) revealed an enrichment of pathways associated with metastatic potential, including GTPase signaling, ECM interactions, angiogenesis, and proliferation (Figure 3G; Table S2) in CD13-overexpressing cells.

Together, these findings demonstrate that CD13 promotes early cancer cell seeding in the brain, independent of evident TME alterations, and underscores its specific function during the initial colonization phase of metastasis.

CD13 is overexpressed in a subset of human BrMs

Given the effect of targeting CD13 in our murine analyses, we next examined its expression in human BrM samples. Using IF staining, we analyzed CD13 protein levels in non-tumor brain tissue and BrMs originating from breast, lung, and melanoma primary tumors (Figure 4A; Table S3). To distinguish CD13 expression across different cell types, we used CD31 and PDGFRβ as vascular markers and CD45 as a pan-immune cell marker and defined $CD31^-PDGFR\beta^-CD45^-$ cells as cancer cells. We found that a subset of breast- and lung-derived BrMs exhibited substantial CD13 overexpression, specifically in the cancer cell population, compared with non-tumor brain tissue, accounting for approximately 30% of all samples analyzed (Figures 4B and 4C). Notably, none of the melanoma BrMs analyzed showed cancer cell CD13 overexpression (Figure 4B). Across all BrM samples—breast, lung, and melanoma—CD13 was also expressed in the vasculature (defined as the $CD31^+$ and/or $PDGFR\beta^+$ areas) (Figures S5A and S5B) and in a subset of infiltrating immune cells (Figures S5A and S5C). However, these non-cancer cell expression patterns were consistent across tumor types and did not differ significantly. To further quantify the proportion of cancer cells expressing CD13, we performed IF analysis in a subset of $CD13^+$ tumors, including a pan-cytokeratin marker to label cancer cells, along with ER-TR7 and CD31 to exclude fibroblasts and ECs, respectively, and CD13 (Figure 4D).

(C) Quantification of control ($n = 8$) and CD13 knockdown ($n = 8$) cancer cells in the brain 48 h after intracardiac injection. Data are represented as mean ± SEM. Each dot represents an individual mouse. An unpaired two-tailed *t* test was used for statistical analysis.
(D) Experimental design for cell transduction, cell labeling, and intracardiac cell injection in gain-of-function cell seeding assays.
(E) Representative flow cytometry plots of control and CD13-OE (overexpressing) cancer cells in the brain 48 h after intracardiac injection, defined by Epcam+FITC+ staining.
(F) Quantification of control ($n = 10$) and CD13-OE ($n = 12$) cancer cells in the brain 48 h after intracardiac injection. Data are represented as mean ± SEM. Each dot represents an individual mouse. A Mann-Whitney test was used for statistical analysis.
(G) Dot plot representation of the normalized enrichment score (NES) of selected positively enriched gene sets from the Hallmark, Reactome, and/or GOBP databases in PyMT-BrM3 CD13-OE vs. control cells (GSEA, cutoff: *P.adj* <0.05).
p values in (C) and (F): $^{**}p < 0.01$, $^{***}p < 0.001$.
See also Figure S4 and Table S2.

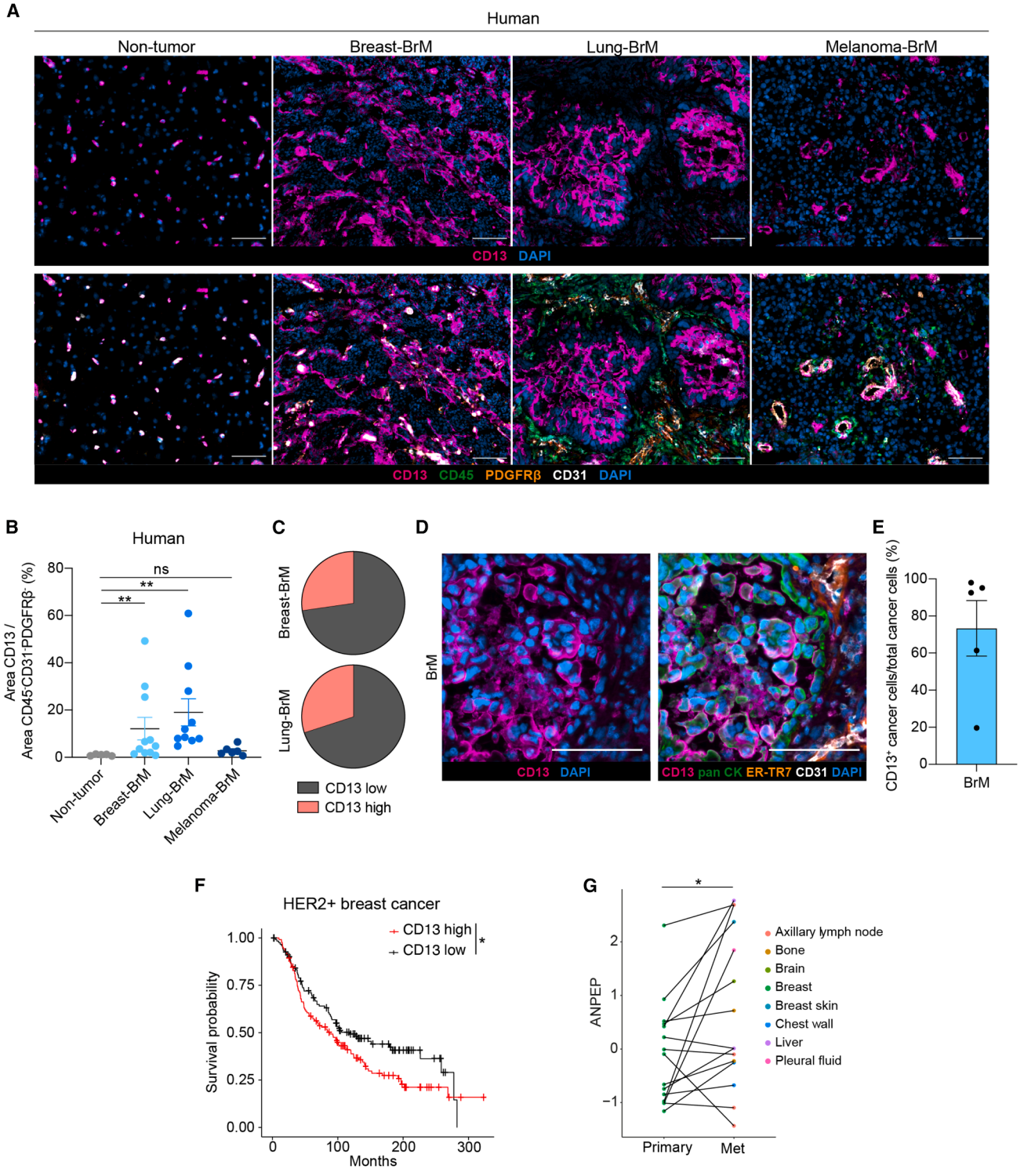

Figure 4. CD13 expression in human BrM

(A) Representative IF images of CD13, CD31 (ECs), PDGFRβ (mural cells), and CD45 (immune cells) in human non-tumor brain tissue samples and BrMs from breast, lung, or melanoma primary origin. Scale bars, 100 μm.

(B) Quantification of $CD13^+$ area in the $CD31^-PDGFR\beta^-CD45^-$ population (cancer cells) in human non-tumor brain samples ($n = 5$) and BrMs from breast ($n = 11$), lung ($n = 10$), or melanoma ($n = 6$) primary origin. Data are represented as mean ± SEM. Each dot represents an individual patient sample. An ANOVA/Kruskal-Wallis test ($p = 0.0019$) was used, followed by a Mann-Whitney two-tailed test with the Bonferroni correction method for multiple comparisons.

(legend continued on next page)

This analysis revealed that an average of ~73% of cancer cells expressed CD13 (Figure 4E), with no spatial preference between perivascular and non-perivascular regions (Figure S5D).

To determine whether CD13 expression is also altered in primary tumors, we analyzed transcriptomic data from publicly available breast and lung cancer cohorts. In BC datasets (The Molecular Taxonomy of Breast Cancer International Consortium (METABRIC) and Metastatic Breast Cancer Project [MBC]; see STAR Methods), CD13 expression did not vary by tumor stage (Figure S5E). By contrast, CD13 levels differed significantly across receptor subtypes, including estrogen receptor positive (ER+), progesterone receptor positive (PR+), human epidermal growth factor 2 (HER2+), and TNBC (Figure S5F). TNBC samples showed the highest median CD13 expression (Figure S5F). In patients with $HER2^+$, specifically, high CD13 expression was associated with reduced survival probability (Figures 4F and S5G). Furthermore, analysis of matched primary breast tumors and metastases from various sites—including brain, bone, lymph node, and liver—revealed significantly higher CD13 expression in metastases, including the one in the brain (Figure 4G).

In contrast, analysis of primary lung cancer samples (The Cancer Genome Atlas [TCGA] and UCologne cohorts; see STAR Methods) revealed no significant variation in CD13 expression by tumor stage (Figure S5H) and no association between CD13 levels and patient survival (Figure S5I).

DISCUSSION

Despite decades of intensive research aimed at developing effective therapeutic strategies, metastasis remains the leading cause of cancer-related mortality worldwide. Among metastatic sites, the brain represents a particular challenge for metastatic colonization due to the presence of the BBB and its tightly regulated vasculature.[8,9] Cancer cells must employ specialized mechanisms to cross the multiple protective layers of the brain vasculature and establish viable colonies within this unique tissue microenvironment.[10–13] These barriers, combined with the limited penetration of many therapeutics across the BBB[26] and the immunosuppressive milieu characteristic of brain tumors,[27–29] significantly hinder effective treatment.[30] Thus, elucidating the molecular drivers of early brain metastatic colonization is crucial for the development of preventative therapeutic approaches.

In this study, we identified the aminopeptidase CD13 as a key mediator in a subset of human BrMs originating from breast and lung cancers, with approximately 30% of samples exhibiting cancer cell-specific CD13 expression. Notably, this prevalence aligns with previous reports in breast and lung primary tumors. In BC, CD13 cancer cell expression was documented in 36% of patient samples analyzed, with higher rates in invasive ductal carcinoma,[31] while in lung cancer, 35% of patients analyzed were positive for cancer cell CD13 expression.[32] These observations suggest that CD13 expression is maintained during metastatic progression to the brain, underscoring its potential as a therapeutic target. Importantly, CD13 expression in primary lung cancer is associated with significantly reduced survival, with a similar trend in BC.[31,32] Consistent with these data, we show here that patients with HER2+ BC with $CD13^{high}$ tumors have significantly poorer clinical outcomes. These findings emphasize the importance of stratifying patients by CD13 status to better assess both its prognostic significance and therapeutic potential.

To gain mechanistic insight into CD13 function, we employed murine BrM models from three primary origins (breast, lung, and melanoma) that recapitulate distinct stages of the metastatic cascade. Notably, only the breast-BrM model exhibited robust CD13 expression, suggesting that lung cancer and melanoma may rely on alternative, CD13-independent mechanisms to colonize the brain. CD13 knockdown in breast-BrM cells significantly prolonged survival and reduced metastatic seeding following intracardiac injection. This effect was less pronounced when cancer cells were introduced directly into the brain parenchyma (intracranial injection) or implanted at the primary site (MFP), underscoring CD13's predominant role during the initial colonization phase of metastasis.

Both gain- and loss-of-function experiments confirmed CD13's functional importance in metastatic seeding. CD13 has been described as a moonlighting enzyme with diverse cellular functions relevant to regulating metastasis,[16,17] including β1 integrin recycling,[21] cell migration,[21] and activation of the MAPK and PI3K pathways.[33] Based on our RNA-seq analysis, CD13 overexpression may further enhance metastatic efficiency through activation of Rho family GTPases and effectors that orchestrate cytoskeletal remodeling, endothelial cell adhesion, and transendothelial migration.[34] These features position CD13 as a compelling anti-cancer target; indeed, CD13 inhibition has been explored in several therapeutic development efforts. However, no brain-permeable CD13 inhibitor has yet been approved worldwide for clinical use,[16] representing a critical gap in the translational landscape.

In summary, we show that CD13 is not only overexpressed in a substantial subset of breast and lung BrMs but also functionally promotes brain metastatic seeding. These findings

(C) Proportion of breast- and lung-derived BrMs with high CD13 expression (threshold: area CD13/area tumor cells >20%), and CD13 low for the remainder.
(D) Representative IF images of CD13, pan cytokeratin (pan CK; cancer cells), ER-TR7 (fibroblasts), and CD31 (ECs) in human non-tumor brain tissue samples and BrMs from breast, lung, or melanoma primary origin. Scale bars, 100 μm.
(E) Quantification of the percentage of $CD13^+$ cancer cells from total cancer cells (defined as pan CK^+; $CD31^-$; ER-$TR7^-$ cells) in BrM ($n = 5$). Data are represented as mean ± SEM. Each dot represents an individual patient sample.
(F) Survival proportions in patients with HER2+ breast cancer with high or low CD13 expression, with expression data split at the median. A Mantel-Cox test was used for statistical analysis.
(G) CD13 expression (Z score) in matched primary breast ($n = 14$) and metastasis samples ($n = 13$). A paired t test was used for statistical analysis. Note that one patient had two primary tumors, resulting in a higher number of primary samples, and that there is only one matched BrM sample.
P.adj values in (B), p values in (G): $^*p < 0.05$, $^{**}p < 0.01$, ns = non-significant.
See also Figure S5 and Table S3.

support the concept of CD13 as a promising therapeutic target for both the prevention and treatment of BrMs. Future efforts should prioritize the development of brain-penetrant CD13 inhibitors to enable the clinical translations of these discoveries.

Limitations of the study

While we provide robust evidence of CD13 expression in cancer cells from breast and lung human BrMs, CD13 was not detected in melanoma-derived BrMs. However, the limited size of our melanoma BrM cohort may restrict the ability to detect rare CD13-positive cases, and additional studies with larger sample sets are warranted. Furthermore, among the three preclinical BrM models analyzed, only the breast-BrM model exhibited cancer cell CD13 expression, limiting our functional experiments to this setting. Future studies should explore whether alternative *in vivo* models or patient-derived xenografts could reveal additional context-specific roles for CD13. Finally, although our data demonstrate that CD13 expression is induced *in vivo*, the specific microenvironmental or mechanical cues responsible for this regulation remain to be determined, representing an important direction for future research.

RESOURCE AVAILABILITY

Lead contact

Further information and requests for resources should be directed to and will be fulfilled by the lead contact, Johanna A. Joyce (johanna.joyce@unil.ch).

Materials availability

This study did not generate new unique reagents.

Data and code availability

- Data: mouse raw RNA-seq data are available at ArrayExpress: RNA-seq analysis on wild-type and CD13 overexpressing breast-BrM cells. ArrayExpress: E-MTAB-15829. Link: https://www.ebi.ac.uk/biostudies/ArrayExpress/studies/E-MTAB-15829?key=f69153e6-0f70-4b5e-a89b-aba7d9ae954e. RNA-seq analysis on breast-BrM cells *in vitro* versus *in vivo*. ArrayExpress: E-MTAB-15830. Link: https://www.ebi.ac.uk/biostudies/ArrayExpress/studies/E-MTAB-15830?key=cf51e0e0-9816-4c48-b03a-5885e949b206.
- Code: this paper does not report any original code.
- Other items: this paper does not report any other items.

ACKNOWLEDGMENTS

We would like to thank all patients who generously donated tissue for this study, as well as the Departments of Neurosurgery, Neuro-oncology, and Pathology at CHUV Lausanne and members of the Joyce and Hegi labs for coordinating tissue collection. We are grateful to all Joyce lab members for stimulating scientific discussions. We thank the mouse pathology facilities, animal facilities, and flow cytometry core facilities of UNIL for excellent technical support and advice. This research was supported in part by the Swiss National Science Foundation Advanced Grant TMAG-3_209224, the Ludwig Institute for Cancer Research, the University of Lausanne, the Carigest Foundation, and the Breast Cancer Research Foundation (to J.A.J.). L.B. was supported by postdoctoral fellowships from the European Molecular Biology Organization (ALTF 1193–2018), the Human Frontier Science Program (LT000038/2019), and the Mark Foundation Momentum Fellowship. R.S.M. was supported by the European Union's Horizon 2020 research and innovation program under the Skłodowska Curie grant agreement (grant agreement 955951, Evomet ITN).

AUTHOR CONTRIBUTIONS

L.B. and J.A.J. conceived the study, designed experiments, and interpreted data. L.B. performed the majority of the experiments and analyses with technical support from R.S.M., E.L., and M.B. A.H.-B. performed the experiments and analyses for the revision of the manuscript, with support from C.F.C. V.R. and N.F. performed the bioinformatic analyses. M.E.H. coordinated the collection of human tissue. L.B. prepared the figures. L.B. and J.A.J. wrote the manuscript. J.A.J. supervised the study. All authors reviewed, edited, or commented on the manuscript.

DECLARATION OF INTERESTS

At the time of publication, L.B. was affiliated with the Biogipuzkoa Health Research Institute, San Sebastian, Spain, and E.L. was affiliated with the Swiss Federal Institute of Technology Lausanne (EPFL), Lausanne, Switzerland. M.E.H. has an advisory role at TME Pharma. J.A.J. received honoraria for speaking at a research symposium organized by Bristol Meyers Squibb and for serving on an advisory board for T-Knife Therapeutics and has previously served on the scientific advisory board of Pionyr Immunotherapeutics (disclosures for the past 3 years).

STAR★METHODS

Detailed methods are provided in the online version of this paper and include the following:

- KEY RESOURCES TABLE
- EXPERIMENTAL MODEL AND STUDY PARTICIPANT DETAILS
  - Human subjects
  - Mouse models
  - Cell lines
- METHOD DETAILS
  - Immunofluorescence staining
  - Analysis of human Anpep expression in public datasets
  - Extracellular matrix coating
  - 3D cell cultures: Matrigel and hanging spheres
  - Flow cytometry analysis of CD13 levels and sorting
  - Lentivirus transduction
  - RNA extraction and real-time PCR
  - Generation of experimental brain metastasis by intracardiac or intracranial injection
  - Mouse monitoring by magnetic resonance imaging (MRI)
  - Generation of mammary fat pad tumors
  - Brain seeding experiments
  - RNA-sequencing
  - Image analysis
- QUANTIFICATION AND STATISTICAL ANALYSIS

SUPPLEMENTAL INFORMATION

Supplemental information can be found online at https://doi.org/10.1016/j.celrep.2025.116895.

Received: May 22, 2025
Revised: November 4, 2025
Accepted: December 23, 2025
Published: January 21, 2026

REFERENCES

1. Valiente, M., Anders, C., Boire, A., Izar, B., Kotecki, N., Malladi, S., Massagué, J., Moss, N.S., Neman, J., Preusser, M., et al. (2025). The evolving landscape of brain metastasis: volume II. Trends Cancer. https://doi.org/10.1016/J.TRECAN.2025.11.007.

2. Steindl, A., Brunner, T.J., Heimbach, K., Schweighart, K., Moser, G.M., Niziolek, H.M., Moor, E., Kreminger, J., Starzer, A.M., Dieckmann, K., et al. (2022). Changing characteristics, treatment approaches and survival of patients with brain metastasis: data from six thousand and thirty-one individuals over an observation period of 30 years. Eur. J. Cancer *162*, 170–181. https://doi.org/10.1016/j.ejca.2021.12.005.

3. Valiente, M., Ahluwalia, M.S., Boire, A., Brastianos, P.K., Goldberg, S.B., Lee, E.Q., Le Rhun, E., Preusser, M., Winkler, F., and Soffietti, R. (2018). The Evolving Landscape of Brain Metastasis. Trends Cancer *4*, 176–196. https://doi.org/10.1016/j.trecan.2018.01.003.

4. Eichler, A.F., Chung, E., Kodack, D.P., Loeffler, J.S., Fukumura, D., and Jain, R.K. (2011). The biology of brain metastases—translation to new therapies. Nat. Rev. Clin. Oncol. *8*, 344–356. https://doi.org/10.1038/nrclinonc.2011.58.

5. Quail, D.F., and Joyce, J.A. (2013). Microenvironmental regulation of tumor progression and metastasis. Nat. Med. *19*, 1423–1437. https://doi.org/10.1038/nm.3394.

6. de Visser, K.E., and Joyce, J.A. (2023). The evolving tumor microenvironment: From cancer initiation to metastatic outgrowth. Cancer Cell *41*, 374–403. https://doi.org/10.1016/j.ccell.2023.02.016.

7. Quail, D.F., and Joyce, J.A. (2017). The Microenvironmental Landscape of Brain Tumors. Cancer Cell *31*, 326–341. https://doi.org/10.1016/j.ccell.2017.02.009.

8. Arvanitis, C.D., Ferraro, G.B., and Jain, R.K. (2020). The blood–brain barrier and blood–tumour barrier in brain tumours and metastases. Nat. Rev. Cancer *20*, 26–41. https://doi.org/10.1038/s41568-019-0205-x.

9. Steeg, P.S. (2021). The blood–tumour barrier in cancer biology and therapy. Nat. Rev. Clin. Oncol. *18*, 696–714. https://doi.org/10.1038/s41571-021-00529-6.

10. Sevenich, L., Bowman, R.L., Mason, S.D., Quail, D.F., Rapaport, F., Elie, B.T., Brogi, E., Brastianos, P.K., Hahn, W.C., Holsinger, L.J., et al. (2014). Analysis of tumour- and stroma-supplied proteolytic networks reveals a brain-metastasis-promoting role for cathepsin S. Nat. Cell Biol. *16*, 876–888. https://doi.org/10.1038/ncb3011.

11. Jilaveanu, L.B., Parisi, F., Barr, M.L., Zito, C.R., Cruz-Munoz, W., Kerbel, R.S., Rimm, D.L., Bosenberg, M.W., Halaban, R., Kluger, Y., and Kluger, H.M. (2015). PLEKHA5 as a biomarker and potential mediator of melanoma brain metastasis. Clin. Cancer Res. *21*, 2138–2147. https://doi.org/10.1158/1078-0432.CCR-14-0861.

12. Bos, P.D., Zhang, X.H.F., Nadal, C., Shu, W., Gomis, R.R., Nguyen, D.X., Minn, A.J., Van De Vijver, M.J., Gerald, W.L., Foekens, J.A., and Massagué, J. (2009). Genes that mediate breast cancer metastasis to the brain. Nature *459*, 1005–1009. https://doi.org/10.1038/nature08021.

13. Li, B., Wang, C., Zhang, Y., Zhao, X.Y., Huang, B., Wu, P.F., Li, Q., Li, H., Liu, Y.S., Cao, L.Y., et al. (2013). Elevated PLGF contributes to small-cell lung cancer brain metastasis. Oncogene *32*, 2952–2962. https://doi.org/10.1038/onc.2012.313.

14. Valiente, M., Obenauf, A.C., Jin, X., Chen, Q., Zhang, X.H.-F., Lee, D.J., Chaft, J.E., Kris, M.G., Huse, J.T., Brogi, E., and Massagué, J. (2014). Serpins Promote Cancer Cell Survival and Vascular Co-Option in Brain Metastasis. Cell *156*, 1002–1016. https://doi.org/10.1016/j.cell.2014.01.040.

15. Gan, S., Macalinao, D.G., Shahoei, S.H., Tian, L., Jin, X., Basnet, H., Bibby, C., Muller, J.T., Atri, P., Seffar, E., et al. (2024). Distinct tumor architectures and microenvironments for the initiation of breast cancer metastasis in the brain. Cancer Cell *42*, 1693–1712.e24. https://doi.org/10.1016/J.CCELL.2024.08.015.

16. Lendeckel, U., Karimi, F., Al Abdulla, R., and Wolke, C. (2023). The Role of the Ectopeptidase APN/CD13 in Cancer. Biomedicines *11*, 724. https://doi.org/10.3390/biomedicines11030724.

17. Mina-Osorio, P. (2008). The moonlighting enzyme CD13: old and new functions to target. Trends Mol. Med. *14*, 361–371. https://doi.org/10.1016/j.molmed.2008.06.003.

18. Hashida, H., Takabayashi, A., Kanai, M., Adachi, M., Kondo, K., Kohno, N., Yamaoka, Y., and Miyake, M. (2002). Aminopeptidase N is involved in cell motility and angiogenesis: Its clinical significance in human colon cancer. Gastroenterology *122*, 376–386. https://doi.org/10.1053/gast.2002.31095.

19. Tokuhara, T., Hattori, N., Ishida, H., Hirai, T., Higashiyama, M., Kodama, K., and Miyake, M. (2006). Clinical Significance of Aminopeptidase N in Non–Small Cell Lung Cancer. Clin. Cancer Res. *12*, 3971–3978. https://doi.org/10.1158/1078-0432.CCR-06-0338.

20. Bhagwat, S.V., Lahdenranta, J., Giordano, R., Arap, W., Pasqualini, R., and Shapiro, L.H. (2001). CD13/APN is activated by angiogenic signals and is essential for capillary tube formation. Blood *97*, 652–659. https://doi.org/10.1182/blood.V97.3.652.

21. Ghosh, M., Lo, R., Ivic, I., Aguilera, B., Qendro, V., Devarakonda, C., and Shapiro, L.H. (2019). CD13 tethers the IQGAP1-ARF6-EFA6 complex to the plasma membrane to promote ARF6 activation, β1 integrin recycling, and cell migration. Sci. Signal. *12*, 5938. https://doi.org/10.1126/scisignal.aav5938.

22. Croci, D., Santalla Méndez, R., Temme, S., Soukup, K., Fournier, N., Zomer, A., Colotti, R., Wischnewski, V., Flögel, U., van Heeswijk, R.B., and Joyce, J.A. (2022). Multispectral fluorine-19 MRI enables longitudinal and noninvasive monitoring of tumor-associated macrophages. Sci. Transl. Med. *14*, eabo2952. https://doi.org/10.1126/SCITRANSLMED.ABO2952.

23. Saltarin, F., Wegmüller, A., Bejarano, L., Ildiz, E.S., Zwicky, P., Vianin, A., Spadin, F., Soukup, K., Wischnewski, V., Engelhardt, B., et al. (2023). Compromised Blood-Brain Barrier Junctions Enhance Melanoma Cell Intercalation and Extravasation. Cancers *15*, 5071. https://doi.org/10.3390/cancers15205071.

24. Bejarano, L., Kauzlaric, A., Lamprou, E., Lourenco, J., Fournier, N., Ballabio, M., Colotti, R., Maas, R., Galland, S., Massara, M., et al. (2024). Interrogation of endothelial and mural cells in brain metastasis reveals key immune-regulatory mechanisms. Cancer Cell *42*, 378–395.e10. https://doi.org/10.1016/j.ccell.2023.12.018.

25. McLarnon, J.G. (2021). A Leaky Blood–Brain Barrier to Fibrinogen Contributes to Oxidative Damage in Alzheimer's Disease. Antioxidants *11*, 102. https://doi.org/10.3390/antiox11010102.

26. Wu, D., Chen, Q., Chen, X., Han, F., Chen, Z., and Wang, Y. (2023). The blood–brain barrier: Structure, regulation and drug delivery. Signal Transduct. Target. Ther. *8*, 217–227. https://doi.org/10.1038/s41392-023-01481-w.

27. Klemm, F., Maas, R.R., Bowman, R.L., Kornete, M., Soukup, K., Nassiri, S., Brouland, J.P., Iacobuzio-Donahue, C.A., Brennan, C., Tabar, V., et al. (2020). Interrogation of the Microenvironmental Landscape in Brain Tumors Reveals Disease-Specific Alterations of Immune Cells. Cell *181*, 1643–1660.e17. https://doi.org/10.1016/j.cell.2020.05.007.

28. Friebel, E., Kapolou, K., Unger, S., Núñez, N.G., Utz, S., Rushing, E.J., Regli, L., Weller, M., Greter, M., Tugues, S., et al. (2020). Single-Cell Mapping of Human Brain Cancer Reveals Tumor-Specific Instruction of Tissue-Invading Leukocytes. Cell *181*, 1626–1642.e20. https://doi.org/10.1016/j.cell.2020.04.055.

29. Karimi, E., Yu, M.W., Maritan, S.M., Perus, L.J.M., Rezanejad, M., Sorin, M., Dankner, M., Fallah, P., Doré, S., Zuo, D., et al. (2023). Single-cell spatial immune landscapes of primary and metastatic brain tumours. Nature, 555–555563. https://doi.org/10.1038/s41586-022-05680-3.

30. Suh, J.H., Kotecha, R., Chao, S.T., Ahluwalia, M.S., Sahgal, A., and Chang, E.L. (2020). Current approaches to the management of brain metastases. Nat. Rev. Clin. Oncol. *17*, 279–299. https://doi.org/10.1038/s41571-019-0320-3.

31. Ranogajec, I., Jakić-Razumović, J., Puzović, V., and Gabrilovac, J. (2012). Prognostic value of matrix metalloproteinase-2 (MMP-2), matrix metalloproteinase-9 (MMP-9) and aminopeptidase N/CD13 in breast cancer patients. Med. Oncol. *29*, 561–569. https://doi.org/10.1007/S12032-011-9984-Y.

32. Zhang, Q., Wang, J., Zhang, H., Zhao, D., Zhang, Z., and Zhang, S. (2015). Expression and clinical significance of aminopeptidase N/CD13

in non-small cell lung cancer. J. Cancer Res. Ther. *11*, 223–228. https://doi.org/10.4103/0973-1482.138007.

33. Guo, Q., Jing, F.J., Xu, W., Li, X., Li, X., Sun, J.L., Xing, X.M., Zhou, C.K., and Jing, F.B. (2019). Ubenimex induces autophagy inhibition and EMT suppression to overcome cisplatin resistance in GC cells by perturbing the CD13/EMP3/PI3K/AKT/NF-κB axis. Aging *12*, 80–105. https://doi.org/10.18632/AGING.102598.
34. Rodenburg, W.S., and van Buul, J.D. (2021). Rho GTPase signalling networks in cancer cell transendothelial migration. Vasc. Biol. *3*, R77–R95. https://doi.org/10.1530/VB-21-0008.
35. Pereira, B., Chin, S.F., Rueda, O.M., Vollan, H.K.M., Provenzano, E., Bardwell, H.A., Pugh, M., Jones, L., Russell, R., Sammut, S.J., et al. (2016). The somatic mutation profiles of 2,433 breast cancers refine their genomic and transcriptomic landscapes. Nat. Commun. *7*, 1–16. https://doi.org/10.1038/ncomms11479.
36. George, J., Lim, J.S., Jang, S.J., Cun, Y., Ozretić, L., Kong, G., Leenders, F., Lu, X., Fernández-Cuesta, L., Bosco, G., et al. (2015). Comprehensive genomic profiles of small cell lung cancer. Nature *524*, 47–53. https://doi.org/10.1038/nature14664.
37. Therneau, T.M., and Grambsch, P.M. (2000). Modeling Survival Data: Extending the Cox Model (Springer).
38. Kassambara, A., Kosinski, M., and Biecek, P. (2021). survminer: Drawing Survival Curves using 'ggplot2'. R package version 0.4.9. https://rpkgs.datanovia.com/survminer/index.html.
39. Ogle, D.H., Doll, J.C., Wheeler, A.P., and Dinno, A. (2025). FSA: Simple Fisheries Stock Assessment Methods. R package version 0.9.6. https://fishr-core-team.github.io/FSA/.
40. Ramos, M., Geistlinger, L., Oh, S., Schiffer, L., Azhar, R., Kodali, H., de Bruijn, I., Gao, J., Carey, V.J., Morgan, M., and Waldron, L. (2020). Multiomic Integration of Public Oncology Databases in Bioconductor. JCO Clin. Cancer. Inform. *4*, 958–971. https://doi.org/10.1200/CCI.19.00119.
41. Davis, S., and Meltzer, P.S. (2007). GEOquery: a bridge between the Gene Expression Omnibus (GEO) and BioConductor. Bioinformatics *23*, 1846–1847. https://doi.org/10.1093/bioinformatics/btm254.
42. Meeth, K., Wang, J.X., Micevic, G., Damsky, W., and Bosenberg, M.W. (2016). The YUMM lines: a series of congenic mouse melanoma cell lines with defined genetic alterations. Pigment Cell Melanoma Res. *29*, 590–597. https://doi.org/10.1111/pcmr.12498.
43. Bankhead, P., Loughrey, M.B., Fernández, J.A., Dombrowski, Y., McArt, D.G., Dunne, P.D., McQuaid, S., Gray, R.T., Murray, L.J., Coleman, H.G., et al. (2017). QuPath: Open source software for digital pathology image analysis. Sci. Rep. *7*, 16878. https://doi.org/10.1038/s41598-017-17204-5.
44. Schmidt, U., Weigert, M., Broaddus, C., and Myers, G. (2018). Cell Detection with Star-Convex Polygons. In Medical Image Computing and Computer Assisted Intervention – MICCAI 2018, A.F. Frangi, J.A. Schnabel, C. Davatzikos, C. Alberola-López, and G. Fichtinger, eds. (Springer), pp. 265–273. https://doi.org/10.1007/978-3-030-00934-2_30.

STAR★METHODS

KEY RESOURCES TABLE

REAGENT or RESOURCE	SOURCE	IDENTIFIER
Antibodies		
IF: anti-mouse CD31 (goat polyclonal)	RD Systems	Cat#AF3628; RRID:AB_2161028
IF: anti-mouse CD31 (rat monoclonal ER-MP12)	Bio-Rad	Cat# MCA2388GA; RRID:AB_2161024
IF: anti-human CD13 (rabbit monoclonal EPR4059)	Abcam	Cat# AB108382; RRID: AB_10890797
IF: anti-mouse CD13 (goat polyclonal)	R&D Systems	Cat#AF2335; RRID:AB_2227288
IF: anti-human CD31 (sheep polyclonal)	R&D Systems	Cat# AF806; RRID:AB_355617
IF: anti human CD45-AF488 (mouse monoclonal HI30)	Biolegend	Cat# 304017; RRID:AB_389314
IF: anti-human PDGFRβ/CD140b-PE (mouse monoclonal 28D4)	BD	Cat# 558821; RRID:AB_397132
IF: anti-human/mouse Fibrinogen (rabbit polyclonal)	Agilent Technologies	Cat# A008002-2; RRID:AB_578481
IF: anti-mouse Ki67 (rabbit monoclonal SP6)	Abcam	Cat# ab16667; RRID:AB_302459
IF: anti-mouse CD45-FITC (rat monoclonal 30-F11)	BD	Cat#553080; RRID:AB_394610
IF: anti-human CD45-AF488 (mouse monoclonal HI30)	BioLegend	Cat#304017; RRID:AB_389314
IF: anti-mouse Iba-1 (rabbit polyclonal)	Wako	Cat#019–19741; RRID:AB_839504
IF: anti-mouse CD8a-AF647 (rat monoclonal 53–6.7)	BioLegend	Cat#100724; RRID:AB_389326
IF: anti-mouse CD3-AF750 (rat monoclonal 17A2)	RD Systems	Cat#FAB4841S-025; RRID: N/A
IF: anti-mouse CD45-PE (30F11)	BioLegend	Cat#103106; RRID:AB_312971
IF: anti-human Pan Cytokeratin (mouse monoclonal AE1+AE3)	Thermo Fisher	Cat#CF190321; RRID: N/A
IF: anti-mouse/human ER-TR7 (rat monoclonal ER-TR7)	Novus Biologicals	Cat# NB100-64932; RRID: AB_963381
IF: anti-mouse EpCAM (rabbit polyclonal)	Abcam	Cat# ab71916; RRID: AB_1603782
IF: AF647 anti-rabbit IgG (donkey polyclonal)	Invitrogen	Cat#A-31573; RRID:AB_2536183
IF: DyLight755 anti-goat IgG (donkey polyclonal)	Invitrogen	Cat# SA5-10091; RRID:AB_2556671
IF: AF488 anti-rat IgG (donkey polyclonal)	Invitrogen	Cat#A21208; RRID:AB_2535794
IF: AF488 anti-goat IgG (donkey polyclonal)	Invitrogen	Cat#A11055/A32814; RRID:AB_2534102/ AB_2762838
IF: AF750 anti-sheep IgG (donkey polyclonal)	Abcam	Cat#ab175756; RRID: N/A
IF: DyLight650 anti-rat IgG (donkey polyclonal)	Invitrogen	Cat# SA5-10029; RRID: AB_2556609
IF: AF488 anti-rabbit (donkey polyclonal)	Invitrogen	Cat# A21206; RRID: AB_2535792
IF: AF488 anti-sheep (donkey polyclonal)	Invitrogen	Cat#A11015; RRID:AB_2534082
IF: AF555 anti-rat (donkey polyclonal)	Abcam	Cat#ab150154; RRID:AB_2813834
IF: AF755 anti-goat (donkey polyclonal)	Invitrogen	Cat#SA5-10091; RRID:AB_2556671
IF: DAPI (4′,6-Diamidino-2-Phenylindole, Dihydrochloride)	Invitrogen	Cat#D1306; RRID:AB_2629482
FCM: anti-mouse CD11b BUV661 (rat monoclonal M1/70)	BD	Cat#612977; RRID:AB_2870249

(*Continued on next page*)

Continued

REAGENT or RESOURCE	SOURCE	IDENTIFIER
FCM: anti-mouse CD45 PerCP/Cy5.5 (rat monoclonal 30-F11)	BioLegend	Cat# 103132; RRID: AB_893340
FCM: anti-mouse CD326 (Ep-CAM) BV421 (rat monoclonal G8.8)	BioLegend	Cat#118225; RRID:AB_2563983
FCM: anti-mouse CD13 BV605	BD	Cat# 740359; RRID:AB_2740091
FCM: Zombie NIR Fixable Viability Dye	BioLegend	Cat#423105
FCM: Purified Rat Anti-Mouse CD16/CD32 (Mouse Fc Block) (rat monoclonal 2.4G2)	BD	Cat# 553142; RRID:AB_394657
Biological samples		
Non-tumor and brain metastasis tissue	Center Hospitalier Universitaire Vaudois, Lausanne, Switzerland	N/A
Chemicals, peptides, and recombinant proteins		
Tween 20 for molecular biology	Applied Chemicals	Cat#A4974
Triton X-100	Applied Chemicals	Cat#A4975
2-Methylbutane	Sigma-Aldrich	Cat#59070
Paraformaldehyde (PFA) 32% solution, EM grade	Electron Microscopy Sciences	Cat#15714-S
Sodium phosphate dibasic (Na_2HPO_4)	Sigma-Aldrich	Cat# S5136
Sodium Phosphate Monobasic, Dihydrate ($NaH_2PO_4{\cdot}2H_2O$)	JT Baker	Cat#JTB-3819-01
L-Lysine	Sigma-Aldrich	Cat#62840
Methanol, 99.9%	Thermo Fisher	Cat#176840025
Fetal Bovine Serum (FBS)	Gibco, ThermoFisher	Cat#10270106
Percoll	Sigma-Aldric	Cat#P1644-100ML
Bovine Serum Albumin	Jackson ImmunoResearch	Cat#001-000-162
Tissue-Tek O.C.T. Compound	Sakura Finetek	Cat# 4583
Donkey Serum	Sigma Aldrich	Cat#S30-M
Fluorescence Mounting Medium	Dako	Cat#S302380-2
Pentobarbital	CHUV	N/A
D(+)-Sucrose for molecular biology	PanReac AppliChem	Cat#A2211,1000
DMEM/F-12, GlutaMAX Supplement	Gibco, ThermoFisher	Cat#31331028
Penicillin-Streptomycin (10,000 U/mL)	Gibco, ThermoFisher,	Cat#15140122
Gadovist (Gadobutrol)	Bayer	N/A
UltraPure 0.5M EDTA	Invitrogen, ThermoFisher	Cat#15575020
Trypan Blue Solution, 0.4%	Gibco, ThermoFisher	Cat#15250061
Brilliant Stain Buffer	BD	Cat#563794
Trypsin-EDTA (0.05%), phenol red	Gibco, ThermoFisher	Cat#25300062
Attane Isoflurane	Attane	N/A
Matrigel	Corning	Cat#356231
Collagen-I	Corning	Cat#354249
Collagen-IV	Cultrex	Cat#3410-010-02
Fibronectin	Advance biomatrix	Cat#5050
Laminin	Corning	Cat#354232
High molecular weight hyaluronan	R&D Systems	Cat#GLR002
Neuroglycan C/CSPG5	R&D Systems	Cat#5665-NG-050
Cell recovery solution	Corning	Cat#354253
CD13 shRNA vectors	Horizon	Cat#RMM3981-201761394 and RMM3981-201761395
CD13 overexpression vector	Sino Biological	Cat#MG50001-ACGLN and LVCV-01

(*Continued on next page*)

Continued

REAGENT or RESOURCE	SOURCE	IDENTIFIER
Protamine	Sigma-Aldrich	Cat#P4020
Puromycin	Millipore	Cat#540411
TaqMan Universal PCR Master Mix	Applied Biosystems	Cat#4324020
CellTracker Green CMFDA	Invitrogen	Cat#C7025
Critical commercial assays		
Brain Tumor Dissociation Kit	Milteny	Cat#130-095-942
RNeasy Mini kit	QIAGEN	Cat#74104
High-Capacity cDNA Reverse Transcription Kit	Applied Biosystems	Cat#4368814
Deposited data		
METABRIC cohort	Pereira et al.[35]	https://cbioportal-datahub.s3.amazonaws.com/brca_metabric.tar.gz
RNA-seq and microarray LUAD, LUSC	TCGA	https://gdac.broadinstitute.org/runs/stddata__2016_01_28/data/LUAD/20160128/https://gdac.broadinstitute.org/runs/stddata__2016_01_28/data/LUSC/20160128/
U Cologne Small-Cell Lung Cancer Dataset	George et al.[36]	https://cbioportal-datahub.s3.amazonaws.com/sclc_ucologne_2015.tar.gz
The Metastatic Breast Cancer Project (MBC)	N/A	https://mbcproject.org/https://cbioportal-datahub.s3.amazonaws.com/brca_mbcproject_2022.tar.gz
RNA-seq analysis on breast BrM cells *in vitro* versus *in vivo*	This paper	ArrayExpress: E-MTAB-15829
RNA-seq analysis on wild-type and CD13 overexpressing breast BrM cells	This paper	ArrayExpress: E-MTAB-15830
Experimental models: Cell lines		
PyMT-BrM3 (breast-BrM)	Joyce lab (Croci et al.[22])	N/A
Sv2T3-BrM1 (lung-BrM)	Joyce lab (Bejarano et al.[24])	N/A
Yumm1.1-BrM4 (melanoma-BrM)	Joyce lab (Saltarin et al.[23])	N/A
Experimental models: Organisms/strains		
C57BL/6J mice	Charles River	N/A
PDGFRβ-CreERT2-R26Tom mice	Joyce lab (Bejarano et al.[24])	N/A
Software and algorithms		
GraphPad Prism (version 8.1.0)	GraphPad software	https://www.graphpad.com/scientific-software/prism/
FlowJo (version 10.7.2)	BD Biosciences	https://www.flowjo.com/
R (version 4.3.2)	The R Foundation	https://cran.r-project.org/
Survival (R package, version 3.5–7)	Therneau and Grambsch[37]	https://cran.r-project.org/package=survival
Survminer (R package, version 0.4.9)	Kassambara et al.[38]	https://rpkgs.datanovia.com/survminer/index.html
FSA (R package, version 0.9.6)	Ogle et al.[39]	https://fishr-core-team.github.io/FSA
cBioPortalData (R package, version 2.14.2)	Ramos et al.[40]	https://ascopubs.org/doi/pdf/10.1200/CCI.19.00119
GEOquery (R package, version 2.70.0)	Davis and Meltzer[41]	https://academic.oup.com/bioinformatics/article/23/14/1846/190290
Other		
gentleMACS Octo Dissociator with Heaters	Miltenyi	Cat#130-096-427
gentleMACS C Tubes	Miltenyi	Cat#130-096-334

(*Continued on next page*)

Continued

REAGENT or RESOURCE	SOURCE	IDENTIFIER
MoFlo Astrios EQ	Beckman Coulter	N/A
BD FACSAria II	BD	N/A
Axio Scan.Z1 slide scanner	Zeiss	N/A
Tissue-Tek Cryomold Standard	Sakura Finetek	Cat#4557
Rectangular cover glasses	Menzel Gläser, VWR	Cat#631-1339
Multifly needle, 25G x 3/4″, 80 mm	Sarsted	Cat#85.1642.005
LSRFortessa flow cytometer	BD	N/A

EXPERIMENTAL MODEL AND STUDY PARTICIPANT DETAILS

Human subjects

Clinical human tissue samples were processed in accordance with the ethical standards of the institutional and/or national research committees and with the 1964 Helsinki declaration and its later amendments or comparable ethical standards. All participants included in this study provided informed consent. The collection of tumor tissue at the Biobank of the Brain and Spine Tumor Center (BB_031_BBLBGT) and Lundin Family Brain Tumor Center of the Center Hospitalier Universitaire Vaudois (CHUV, Lausanne, Switzerland) was approved by the Commission Cantonale d'éthique de la recherche sur l'être humain (CER-VD, protocol PB 2017–00240, F25/99). As part of standard clinical care, pathological review of tumor tissues was performed at CHUV; comprehensive clinical information is detailed in Table S1.

Mouse models

The Institutional Animal Care and Use Committees of the University of Lausanne and Canton Vaud, Switzerland, granted approval for all animal studies, with license numbers VD3314 and VD3688. Mice were accommodated in individually ventilated cages in the Agora *In Vivo* Center (AIVC) animal facility, following a 12h light/dark schedule at 22°C. Mice had continuous access to standard autoclaved lab diet and water. C57BL/6J mice were purchased from Charles River Laboratories. PDGFRβ-CreERT2-R26Tom mice (C57BL/6J background) generated in our previous studies[24] were used for mural cell labeling.

Cell lines

PyMT-BrM3 (breast-BrM), Sv2T3-BrM1 (lung-BrM), Yumm1.1-BrM4 (melanoma-BrM) and 293T cell lines were cultured in DMEM-F12 (1:1) + Glutamax (Gibco) supplemented with 10% fetal bovine serum (FBS, Gibco) and 1% penicillin/streptomycin (P/S, Gibco). The three cell lines were maintained under adherent conditions. The Sv2T3-BrM1 cell line was cultured in 30 μL hanging drops in an inverted plate 12h prior to injection (see section of *Generation of experimental brain metastasis).* PyMT-BrM3 were culture in 30 μL hanging drops to assess CD13 levels (see section *3D cell cultures: Matrigel and hanging spheres*). Every cell line is routinely tested for mycoplasma contamination and confirmed negative before experiments.

The PyMT-BrM3 breast cell line originated from the murine parental 99LN cell line, after three rounds of *in vivo* selection to the brain.[22] The parental cell line was isolated from a metastatic lymph node lesion that arose in the MMTV-PyMT (murine mammary tumor virus; polyoma middle T antigen) breast cancer model, C57BL/6J background. The Yumm1.1-BrM4 melanoma line was established from the Yumm.1.1 cell line[42] after four rounds of *in vivo* selection.[23] The Sv2T3-BrM1 cell line was generated by subjecting a parental line derived from the $Kras^{LSL-G12D/WT}$;$p53^{fl/fl}$ (KP) lung cancer model to one round of *in vivo* passaging to the brain.[24]

METHOD DETAILS

Immunofluorescence staining

Mice were euthanized through terminal anesthesia using pentobarbital, and subsequent intracardiac perfusion was performed with PBS and periodate-lysine-paraformaldehyde (PLP) buffer. Brains were dissected, immersed in PLP for 24h, and changed to 30% sucrose for an additional 24h at 4°C. The tissue was then embedded in OCT and preserved at −80°C for subsequent sectioning at 10 μm thickness and mounting on slides.

Clinical samples were embedded in OCT through immersion in cold 2-methyl butane (Sigma-Aldrich). Samples were stored at −80°C, sectioned at 10 μm thickness and mounted on glass slides. After air-drying, the tissue was fixed in ice-cold 100% methanol (Thermo Fisher) for 10 min and rehydrated with three washes of 5 min each in 1x PBS (Gibco).

Mouse and human tissue sections were permeabilized with 0.2% Triton X-100 (Applied Chemicals) in PBS for 30 min and 3h, respectively, at room temperature (RT); and blocked with 10% normal donkey serum (NDS) (EMD Millipore) in PBS for a minimum of 1h at RT. The blocking buffer was removed, and the tissue was incubated with the primary antibody mix (see Key Resource table) overnight at 4°C, followed by 3 washes of 10 min each with 0.2% Tween (Applied Chemicals) in PBS on a shaker at RT. The secondary

antibody mix (see Key Resource table) and DAPI (Life Technologies) were incubated for 1h at RT, followed by three additional washes (as explained above). If applicable, the slides were incubated with the conjugated antibody mix for 1h at RT and washed three times. In the final step, the slides were mounted using Dako fluorescence mounting medium (Agilent) and covered with a coverslip. An Axio Scan.Z1 slide scanner (Zeiss) was used for imaging using a 20x objective.

Analysis of human Anpep expression in public datasets

Gene expression and clinical data from multiple breast and lung cancer cohorts were integrated to evaluate associations between *Aminopeptidase N (ANPEP)* mRNA expression and tumor grade/stage. Data were sourced from the following publicly available repositories and included both microarray and RNA-seq platforms:

The Molecular Taxonomy of Breast Cancer International Consortium (METABRIC)[35]: This dataset included 2,000+ primary breast tumors with Illumina microarray-derived mRNA z-scores (downloaded on Dec 14th, 2023).

The Cancer Genome Atlas (TCGA): RNA-seq expression data were analyzed in LUAD and LUSC (lung adenocarcinoma/nonsquamous carcinoma, combined $n = 864$ (downloaded on July 17th, 2024).

U Cologne Small-Cell Lung Cancer Dataset[36]: A publicly available cohort provided RNA-seq profiles from 120 SCLC tumors and matched normal lung tissues (downloaded on May 25th, 2023).

The Metastatic Breast Cancer Project (MBC): This dataset release is derived from 379 samples, including both primary and/or metastatic tumor specimens (FFPE) from 301 patients who developed metastatic breast cancer (downloaded on May 25th, 2023).

To harmonize technical variability between platforms, *ANPEP* mRNA expression *Z* score values were used. Shapiro tests indicated non-normal distributions of *ANPEP* expression across tumor grades/stages. Consequently, non-parametric Kruskal-Wallis tests were applied to assess differences in *ANPEP* expression levels among groups within each cohort. Where significant effects ($p < 0.05$) were detected, pairwise comparisons between tumor grades/stages were conducted using Dunn's test with Bonferroni correction for multiple testing. For survival analysis, patients were stratified by *ANPEP* expression median cutoffs to evaluate associations with clinical outcomes. Kaplan-Meier curves and log rank tests were used to assess differences in overall survival (OS). Statistical analyses were performed in R (version 4.3.2) using packages such as 'survival' (version 3.5–7) and 'survminer' (version 0.4.9) for Kaplan-Meier curves, 'FSA' (version 0.9.6) for Dunn's tests, 'cBioPortalData' (version 2.14.2) and 'GEOquery'(version 2.70.0) for data accession.

Extracellular matrix coating

12-MW plates were coated overnight at 4°C with 0.5 mL of Matrigel (Corning) 1% in basal media, collagen-I (Corning) 100 μg/mL in H_2O, collagen-IV (Cultrex) 100 μg/mL in H_2O, fibronectin (Advance biomatrix) 40 μg/mL in PBS, laminin (Corning) 40 μg/mL in PBS, high molecular weight hyaluronan (R&D systems) 100 μg/mL in PBS and neuroglycan C/CSPG5 (R&D systems) 1 μg/mL in PBS. Uncoated wells were used as controls. PyMT-BrM3 cells were incubated for 72h and detached with trypsin to proceed with the FACS protocol as detailed in the section "*Flow cytometry analysis of CD13 levels and sorting".*

3D cell cultures: Matrigel and hanging spheres

For hanging spheres culture, PyMT-BrM3 cells were resuspended at a concentration of 67000 cells/ml and seeded in 30 μL drops on the lid of a p150 plate. The lid was inverted, and cells were incubated for 12h. PBS was added in the bottom of the plate to prevent liquid evaporation. For Matrigel culture, PyMT-BrM3 cells were incubated in 50% Matrigel (Corning) 50% DMEM-F12 (1:1) + Glutamax (Gibco) supplemented 10% FBS and 1% P/S for one week. Matrigel was disrupted with Cell Recovery Solution (Corning) following the manufacturer's instructions. Spheres were dissociated mechanically before proceeding with the FACS protocol as detailed in the section "*Flow cytometry analysis of CD13 levels and sorting".*

Flow cytometry analysis of CD13 levels and sorting

Samples were stained with Zombie NIR fixable viability dye (Biolegend) for 20 min, followed by a 10 min blocking step with Purified Rat Anti-Mouse CD16/CD32 (BD). The antibody mix (see Key Resource Table) was incubated for 15 min in the dark. Samples were washed and resuspended on FACS buffer containing 0.5% BSA (Jackson ImmunoResearch) and 2 mM EDTA (Invitrogen). PyMT-BrM3 cell sorting into CD13-high and CD13-low populations was performed using the multicolor fluorescence-activated cell sorter (BD FACSAria or MoFlo Astrios EQ). Data acquisition was performed using a 5-Laser LSRFortessa flow cytometer (BD). Data was analyzed using FlowJo software (BD).

Lentivirus transduction

For virus production, 293T cells were transfected with VSVG and pPAX2 packaging vectors and the plasmids of interest. For CD13 knockdown experiments, a pLKO non-targeting control and TRC pLKO CD13 shRNAs were used (RMM3981-201761394 clone TRCN0000031087 and RMM3981-201761395 clone TRCN0000031088, Horizon). For overexpression studies, pLV-C-GFPSpark CD13 overexpression vector and the corresponding empty vectors were used (MG50001-ACGLN and LVCV-01, Sino Biological).

PyMT-BrM3 cells were incubated with the viral particles for at least 24h in the presence of protamine (8ug/ml, Sigma-Aldrich) and selected either with puromycin (1ug/ml, Millipore) for the shRNA knockdown or by sorting of GFP^+ cells for CD13 overexpression. Multiple rounds (~3) of sorting were needed to obtain a pure cell population.

RNA extraction and real-time PCR

Total RNA from cells or tumors was extracted with the RNeasy kit (QIAGEN) and reverse transcribed using the High-Capacity cDNA Reverse Transcription Kit (Applied Biosystems), following the manufacturer's instructions. Quantitative real-time PCR was performed with the QuantStudio 6 Flex (Applied Biosystems) using the TaqMan Universal PCR Master Mix (Applied Biosystems) and the TaqMan probes for CD13 (Mm00476227_m1, Mm00476226_g1) and GAPDH (Mm99999915_g1).

Generation of experimental brain metastasis by intracardiac or intracranial injection

For breast- or melanoma-BrM generation in immunocompetent mice, a total of $1x10^5$ PyMT-BrM3 cells or $50x10^3$ Yumm1.1-BrM4 cells (resuspended in HBSS) were inoculated into the left cardiac ventricle of 6–10 weeks old mice (C57BL/6J background). For lung-BrM generation in immunocompetent mice, cells were resuspended at a concentration of 67000 cells/ml in DMEM-F12 (1:1) + Glutamax (Gibco), supplemented with 10% FBS and 1% P/S. Cells were seeded in 30 μL drops in the lid of a Petri dish and incubated for 12h with the lid inverted, to enable the formation of hanging spheres. To prevent evaporation, PBS was added to the Petri dish during the incubation time. To minimize the outgrowth of lung and melanoma cancer cells in the injection site, cancer cells were not directly injected into the heart. Instead, a Multifly-needle (25G, 80mm, SARSTED) with an attached syringe filled with PBS was inserted into the left cardiac ventricle of 6–10 weeks old mice (C57BL/6J background), followed by cancer cell injection into the catheter tube (four hanging drops per mouse) and a flush with PBS.

Mouse monitoring by magnetic resonance imaging (MRI)

Mice were weekly monitored by MRI using a 3 Tesla small animal MR scanner (Bruker BioSpin MRI, Ettlingen, Germany) with an 82-mm volume coil as a transmitter combined with a 2 × 2 mouse brain phased array surface coil for signal reception.

Mice were anesthetized with 2.5% isoflurane (Attane) in oxygen for 1–2 min, followed by injection with 150 μL of gadolinium (Gadovist, 1 mmol/mL,Bayer) as a contrast agent. Anesthesia was maintained throughout the whole procedure, monitoring the respiration rate with a respiration pillow placed bellow the mouse abdomen (SA Instruments, Stony Brook, New York, USA). The body temperature was kept constant at 37.0 ± 0.5°C using a tubing system circulating warm water. Data was acquired with Paravision 360 v2.0 software (Bruker BioSpin MRI, Ettlingen, Germany). To assess the mouse head position, a 3-slice localizer was employed, followed by a T1-FLASH (fast low-angle shot magnetic resonance) sequence with the following parameters: repetition time (TR) = 232.9 ms, echo time (TE) = 5.2 ms, flip angle = 50°, number of averages (NA) = 4, number of slices = 9, slice thickness (ST) = 0.7 mm, field of view (FOV) = 20 × 20 mm^2, matrix size (MS) = 128 × 128, pixel size 0.156 × 0.156 mm^2, acquisition time (Tacq) = 1m33s. Images were acquired in axial planes. Tumor volume was quantified with MIPAV software (National Institutes of Health, USA). Mice were sacrificed when symptoms developed.

Generation of mammary fat pad tumors

PyMT-BrM3 cells were resuspended at a concentration of $7x10^6$ cells/ml in 50% HBSS 50% Matrigel (Corning) and kept on ice until injected. Mice were anesthetized with 2.5% isoflurane (Attane) in oxygen and 100 μL of the cell suspension was injected subcutaneously into the MFP. Tumor growth was monitored over time by biweekly caliper measurements.

Brain seeding experiments

PyMT-BrM3 cells were resuspended at a concentration of $2\text{-}4x10^6$ cells/ml in prewarmed serum free medium. Cel tracker green (Invitrogen) is prepared in serum-free medium at a concentration of 10 μM and added to the PyMT-BrM3 cells in 1:1 ratio for a final concentration of 5 μM. After an incubation of 30 min at 37°C, cells were washed and filtered through a 100 μm strainer with HBSS. Mice were injected intracardially with a total of $5x10^5$ PyMT-BrM3 cells. After 48h, mice were euthanized through terminal anesthesia using pentobarbital and perfused with PBS. The brain tissue was minced for <5 min and digested using the brain tumor dissociation kit (BTDK) in a gentleMACS Octo Dissociator (Miltenyi). Cell suspension was resuspended in 1 mL of PBS, transferred into a tube containing 4 mL of 22% Percoll solution (Sigma-Aldrich) and centrifuged 10 min at 560g without the break on. After centrifugation the supernatant was removed, the cell suspension was washed with PBS (Gibco) and transferred to a FACS tube to proceed with the staining, as described in the section "*Flow cytometry analysis of CD13 levels and sorting*". Data acquisition was performed using a 5-Laser LSRFortessa flow cytometer (BD). Gating was performed on $Zombie^-$ $CD45^-$ $CD11B^-$ cells (to discard dead and immune cells), followed by $Epcam^+GFP^+$ gating to detect seeded cancer cells. The brain-seeded cancer cells are calculated as percentage from $CD45^-$ $CD11B^-$ cells.

RNA-sequencing

In the PyMT-BrM3 *in vivo* vs. *in vitro* analysis, *in vitro* cells were detached from culture plates with Trypsin+0.05% EDTA (Gibco). For the *in vivo* condition, mice bearing BrM at humane endpoint were anesthetized with a lethal dose of pentobarbital, intracardially perfused with 10 mL of ice-cold PBS, and brain metastatic lesions were dissected from surrounding healthy tissue. Single-cell suspensions were generated by dissociating tumors using the Tumor Dissociation Kit (TDK) for mouse (Miltenyi) and the mTDK2 protocol on a gentleMACS Octo Dissociator (Miltenyi).

For both *in vitro* and *in vivo* samples, single-cell suspensions were filtered, counted and stained with Zombie NIR, CD45 and EpCAM fluorescent antibodies. $Zombie^-$ $CD45^-$ $EpCAM^+$ cells were sorted on a MoFlo Astrios EQ. After sorting, cells in ice-cold

complete DMEM/F12 were immediately washed with PBS, pelleted, and immediately stored at −80°C until RNA extraction. RNA purification was performed using the RNeasy Mini kit following the manufacturer's instructions and prepared at a concentration of 5 ng/uL in RNAse-free water. Libraries were prepared using the Illumina TrueSeq stranded mRNA kit and sequenced on an Illumina Novaseq 6000. Raw fastq files were quality-checked, trimmed and aligned to the mouse reference genome mm10 (murine genome version 39 with GENCODE M26 annotation) using STAR (v2.7.9a) and RSEM (RSEM v1.3.1) with default parameters. FPKM values were computed using tximport (v1.20.1). Gene summarized raw counts produced by tximport were processed as follows: non-protein coding genes, pseudogenes, predicted genes, predicted pseudogenes, and genes with FPKM = 0 in all samples were filtered out. The final matrix of 11 samples and 15,420 genes was normalized for library size using the TMM method from EdgeR (v4.2.2) and voom from limma (v3.60.6). Differential expression between groups was computed using limma (lmFit and eBayes), and *p* values were adjusted for multiple testing using the Benjamini-Hochberg method.

In the PyMT-BrM3 CD13-OE vs. control analysis, transfected cell lines were generated as described in the *Lentivirus transduction* section. Cells in culture were detached with Trypsin+0.05% EDTA (Gibco) and RNA extracted using the RNeasy Mini Kit (QIAGEN) according to the manufacturer's instructions. Libraries were prepared using the Watchmaker mRNA protocol and sequenced on an Illumina Novaseq 6000. Raw fastq files were quality-checked, trimmed, and aligned to the mouse reference genome GRCm38 using nf-core/rnaseq (v3.20.0-gb971ba1) pipeline with default parameters. Gene summarized raw counts produced by Salmon (v1.10.3) and tximport (v1.20.1) were processed as follows: genes with low read counts (average TPM <1 or average counts <5 per sample) and non-protein-coding genes were filtered out. The final matrix of 8 samples and 10,697 genes was normalized for library size using the TMM method from EdgeR (v4.2.2) and voom from limma (v3.60.6). Differential expression between groups was computed using limma (lmFit and eBayes), and *p* values were adjusted for multiple testing using Benjamini-Hochberg method. Pathway enrichment was performed with clusterProfiler (v4.12.6) using GSEA and the following gene set collections: Hallmark, Reactome, and Gene Ontology (GO) biological process from msigdbr (v7.5.1).

Image analysis

VIS Image Analysis software (Visiopharm) or QuPath v0.3.0 and v0.5.0[43] image analysis software was used for image analysis.

Visiopharm analysis

For each individual sample, a region of interest (ROI) was manually defined excluding tissue edges and aberrant signals, such as those resulting from tissue folds, dust particles, or air bubbles. To classify objects, detection thresholds were determined based on pixel intensity.

Qupath analysis

For each sample, a ROI was manually defined excluding tissue edges and aberrant signals such as those resulting from tissue folds, dust particles, or air bubbles. Nuclear segmentation was performed with the The StarDist method[44] powered by the dsb2018_heavy_augment.pb deep learning model with the following parameters: threshold = 0.5; channels = 'DAPI'; pixelSize = 0; cellExpansion = 3; cellConstrainScale = 1.5; measureShape = true; measureIntensity = true; includeProbability = true; nThreads = 10. To classify objects, detection thresholds were determined based on pixel intensity. To define the perivascular area, a pixel classifier was generated to perform a mask over the vessels based on CD31 expression. The perivascular area was calculated as the combination of the mask and an expansion of 15 μm diameter from the external border of the mask, excluding objects less than 50 μm^2.

QUANTIFICATION AND STATISTICAL ANALYSIS

GraphPad Prism software and R (v4.3.2) were used for basic statistical analysis. Summary data are presented as mean ± standard error of the mean (SEM). When the data followed a continuous normal distribution, Student's *t* test and ordinary ANOVA were applied; when data distributions failed normality tests the equivalent non-parametric Mann-Whitney and Kruskal-Wallis tests were used. When comparing multiple groups, individual *p*-values were corrected for multiple testing using the Bonferroni correction method unless otherwise stated. Differences were considered statistically significant at $p \leq 0.05$ or $P.adj \leq 0.05$.